PHYSICAL REVIEW RESEARCH **7**, 043129 (2025)

Soliton gas dynamics and rogue wave enhancement in a natural coastal environment

Rodrigo Cienfuegos,[1,2,3,*] Patricio A. Catalán,[4] Raúl P. Flores,[4] Maricarmen Guerra,[2,5] Felipe Lucero,[3]
José Galaz,[1,2] Sander Wahls,[6] Paola Díaz,[1] Rodolfo Gómez,[1] and César Esparza[1,2]
[1]*Departamento de Ingeniería Hidráulica y Ambiental, Escuela de Ingeniería, Pontificia Universidad Católica de Chile, Santiago, Chile*
[2]*Centro de Investigación para la Gestión Integrada del Riesgo de Desastres, Santiago, Chile*
[3]*Marine Energy and Innovation Center, Santiago, Chile*
[4]*Departamento de Obras Civiles, Universidad Técnica Federico Santa María, Valparaíso, Chile*
[5]*Departamento de Ingeniería Civil, Facultad de Ingeniería, Universidad de Concepción, Concepción, Chile*
[6]*Karlsruhe Institute of Technology, Institute of Industrial Information Technology, Karlsruhe, Germany*

(Received 30 November 2023; accepted 23 September 2025; published 3 November 2025)

We document a field experiment in which a path to strongly interacting soliton gas dynamics is observed within an intermittently open/closed estuary. We show that the shallow estuary mouth acts as a low-pass filter for incoming ocean waves, damping energy within the swell frequency band (0.04–1 Hz) and allowing surf-zone generated infragravity waves (frequency band 0.004–0.04 Hz) to enter the semienclosed shallow lagoon formed near the estuary mouth. These long waves penetrate under highly nonlinear conditions with Ursell numbers consistent with multisoliton fission regimes. The k–ω spectrum of the incident wave trains is consistent with solitonic kinematics, demonstrating that solitons are released by the fission of incoming infragravity waves at the lagoon entrance. Continuous injection of solitonic wave trains and intense wave-wave interactions enhanced by the shallow and gradually varying bathymetry within the estuary lagoon lead to a quasistationary soliton gas regime with a substantially increased probability of rogue wave occurrence compared with linear wave theory. The Korteweg-de Vries nonlinear Fourier transform reveals that nearly half of the measured signal energy is explained by solitonic modes, confirming the key role that solitons have in enhancing rogue wave emergence in natural coastal settings.

DOI: 10.1103/9zhq-j1sj

I. INTRODUCTION

Solitons or "waves of translation," as they were first named by J. S. Russell in the 19th century, have resurfaced as a fascinating research object in recent decades. Starting from nonlinear physics [1,2], they have gained interest from a wide spectrum of disciplines such as optics and optical communications [3–6], ocean sciences [7–14], or fluid dynamics [15–17]. Solitons are intriguing waves since their shape and propagation velocity are unchanged due to the balance between nonlinear and dispersive effects. Unlike linear waves, they can also behave akin to particles when they interact with each other through elastic collisions that produce phase shifts at each interaction [2]. These fundamental properties explain the possibility that a dense group of interacting solitons of different amplitudes evolve into a nonlinear random wave field termed soliton gas (SG) [18–20]. Theoretical and numerical studies have demonstrated that one-dimensional integrable systems of partial differential equations, such as the nonlinear Schrödinger or the Korteweg-de Vries (KdV) equations, in deep and shallow waters, respectively, can produce these nonlinear random wave fields [21]. Carefully controlled experiments in optics [22–24], and in water wave tanks [17,25,26], have succeeded in producing and measuring SG. The emergence of rogue waves has also been associated with SG characterized by large-amplitude fluctuations with heavy-tailed non-Gaussian and quasistationary statistics [27–31].

While routes to strongly interacting soliton dynamics have been found under carefully designed numerical and laboratory experiments, field evidence showing that these wave regimes can exist under uncontrolled natural conditions is scarce. The only reported set of field measurements that could be interpreted as a densely distributed set of soliton wave packets is from Ref. [12]. They analyzed low-pass filtered sea surface time series recorded on capacitance-type rods, and identified solitons formed from a wind wave field using the periodic version of the KdV nonlinear Fourier transform (NFT). They showed that the spectral signature of the low-pass filtered signals, with a power-law decay in frequency, was compatible with soliton turbulence [32].

In this article, we present field observations of SG dynamics that lead to a significant increase in the probability of encountering rogue waves compared with linear theory. A description of the study site, the instrumental deployment, and the signal analysis techniques are presented in Sec. II. The contextual oceanographic, hydrographic, and estuarine

---

[*] Contact author: rcienfue@uc.cl

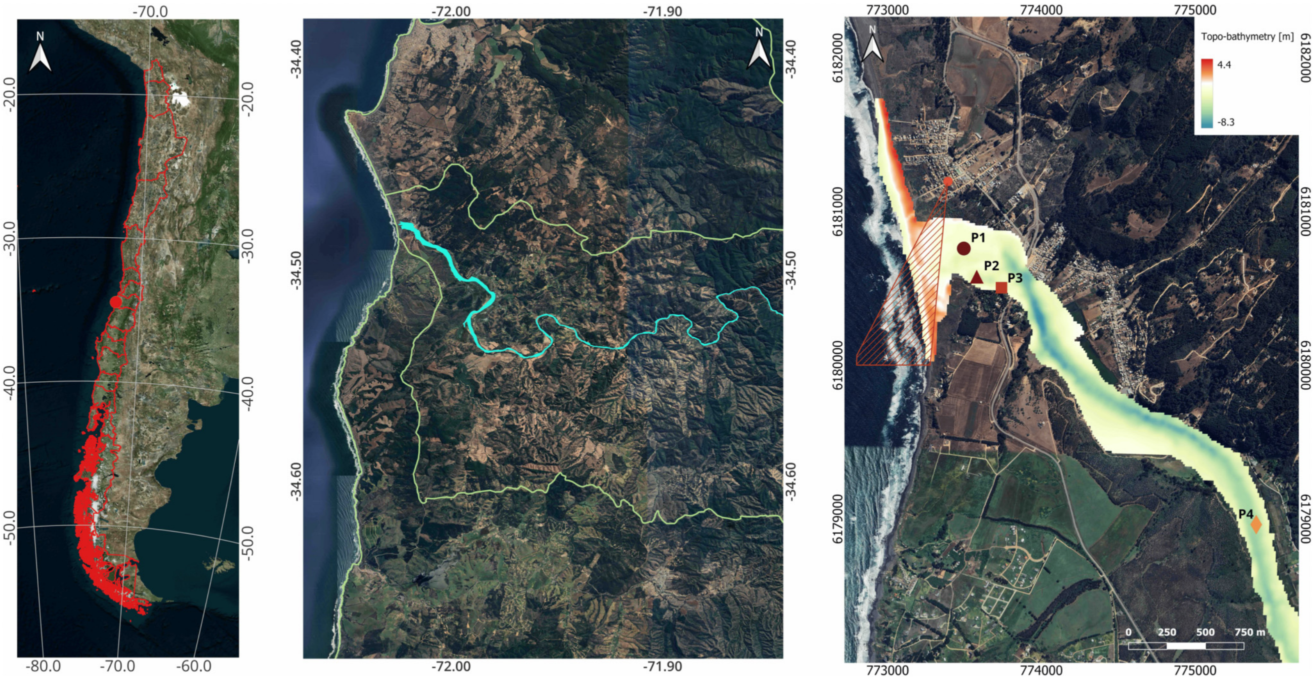

FIG. 1. Laguna Cáhuil at the river mouth of the Nilahue River in the O'Higgins Region, Chile (34.48°S, 72.00°W). Left panel: Location in central Chile. Middle panel: Lower part of the river basin (limits in yellow line) and the main river course (light blue). Right panel: Topobathymetry of the Laguna and the river channel with respect to the mean sea level measured between 24 and 27 March 2023. The locations of the pressure sensors moored during the field campaign are shown in colored symbols (P1 ●, P2 ▲, P3 ■, P4 ◆). The fixed camera's field of vision, used to capture incident ocean wave frequencies, is depicted by the red hatched triangle.

conditions during the field campaign are provided as Supplemental Material [33]. The analysis of the field data is presented in Sec. III, a conceptualization of the conditions that enhanced the observed SG dynamics is given in Sec. IV, and the main conclusions are summarized in Sec. V.

II. MATERIALS AND METHODS

The study site, and methodological details associated with the signal and video processing, and numerical experiments conducted to complement the analysis of the field data are reported in this section.

A. Study site and instrumental deployment

The analyzed dataset is recorded near the outlet of the Nilahue River catchment in Laguna Cáhuil, located on the Pacific coast of central Chile at latitude 34.48°S (Fig. 1), between the 1st and 3rd of August 2023. Laguna Cáhuil is a notable example of an intermittently open/closed estuary, located in a wave-dominated and microtidal mid-latitude setting, where river mouth connections to the ocean occur intermittently following dry and wet seasons [34]. The Nilahue River catchment is a relatively small watershed (area of $1700\,\mathrm{km}^2$ with maximum elevation of 900 masl) draining the coastal mountain range, where a shallow bar-built lagoon system is formed at its river mouth. It is exposed to energetic swells predominantly coming from SW-SSW directions, with mean annual significant waveheight and peak period of $H_{m0} = 2.5\,\mathrm{m}$ and $T_p = 13\,\mathrm{s}$, respectively, and average tidal ranges between 1 and 2 m [35]. Details on hydrographic, oceanographic, and estuarine conditions during the field campaign are provided in the Supplemental Material [33].

In the field experiment, three instruments were moored to capture bottom pressure time series close to the river mouth within the estuary lagoon (P1–P3) and a fourth was placed nearly 3 km upstream in the river channel (P4). Incident ocean wave kinematics was captured using a fixed high-resolution video camera and unmanned aerial vehicles (UAVs). The instrumental deployment is shown in the right panel of Fig. 1; the dataset analyzed below is publicly available at Ref. [36].

B. Instrumental settings and pressure signal processing

The pressure data were gathered using one Aqualogger310 turbidity-pressure sensor (P1 in Fig. 1) and three Nortek Vector acoustic doppler velocimeters (P2–P4 in Fig. 1). The sampling rate for all pressure sensors was set to 1 Hz. The offset for the pressure signals is estimated as the average of the first 1000 data points in the records when the instruments were outside the water. Water surface time series are reconstructed from pressure data using the nonlinear and nonhydrostatic method proposed by Bonneton *et al.* [37] using a constant water density value $\rho = 1.020\ \mathrm{kg/m^3}$ and considering the deployment of the instruments, moored under the mean water depth h and the distances above the bottom δ_m shown in Table I.

Normalized spectrograms are computed with the continuous Morlet wavelet transform following the implementation in Ref. [38] (matlab toolbox available at Ref. [39]).

TABLE I. Distance above the bottom (δ_m) where the pressure sensors were deployed and mean water depth (h), computed over the entire duration of the recorded signals.

Station	P1	P2	P3	P4
δ_m (m)	0	0	0.69	0.58
h (m)	0.25	0.51	2.28	3.62

Water depth signals are high-pass filtered using a Butterworth filter [40] of order 4 with a cutoff frequency of 0.001 Hz (16 min) to study wave motions within the sea-swell-infragravity wave (IGW) frequency band (1 s to 10 min [41–44]). The power spectral density (PSD) is estimated using the Welch method with 512 data points (∼8.5 min) averaged over Hanning windows with an overlap of 50%.

C. Wave-to-wave analysis and high-order statistics of water depth records

A zero-up crossing technique [45] is applied on the high-pass filtered water depth signals to identify individual waveheights. We define the waveheight H as the difference between the maximum and minimum values of the signal between zero crossings. Waveheights are stored if $H > \sigma/5$, where σ is the standard deviation of the time series. The significant waveheight $H_{1/3}$ is computed as the average of the highest one-third waveheights in the record.

The exceedance probability distributions for the waveheights and crest heights in a Gaussian wave field are written as [46]

$$P(H/H_{1/3} > x) = e^{-2x^2}, \tag{1}$$

$$P(\eta_c/H_{1/3} > x) = e^{-8x^2}, \tag{2}$$

and the empirical exceedance probability distributions are computed from the ordered series of the identified waveheights and crest heights.

The kurtosis (Ku) is a measure of the “tailedness” of the probability distribution of the time series, the skewness (Sk) accounts for the horizontal (peaked) asymmetry of the wave signal, and the asymmetry coefficient (As) measures the left-to-right (pitched forward) asymmetry of the wave shapes. They are, respectively, computed as

$$\mathrm{Ku} = \frac{\mu_4}{\sigma^4}, \tag{3}$$

$$\mathrm{Sk} = \frac{\mu_3}{\sigma^3}, \tag{4}$$

$$\mathrm{As} = \frac{\mathcal{H}(\eta)^3}{\sigma^3}, \tag{5}$$

where $\mathcal{H}(\cdot)$ is the imaginary part of the Hilbert transform operator applied to time series, and μ_3 and μ_4 are the third- and fourth-order moments, respectively.

D. Remote sensing of ocean waves reaching the coast and penetrating into Laguna Cáhuil

We use a fixed high-resolution video camera to capture ocean waves reaching the coast and penetrating into the bar-built estuary (see its spatial coverage in Fig. 2). The video acquisition system comprises a microcontroller (Raspberry Pi 4) and a 12.3-megapixel camera (Raspberry Pi HQ), which utilizes a Sony IMX477 sensor in conjunction with a 16 mm focal length Arducam lens. The camera calibration and orthorectification process are conducted following Ref. [47], which entails the determination of both intrinsic and extrinsic parameters of the camera. This procedure is carried out using the OpenCV library in Python [48] with 58 ground control points obtained with a Trimble R3 GPS system, all referenced to the local datum. The full frame images are rectified, and spatial transects are defined at two alongshore locations (TS1 and TS2 shown in Fig. 2) spanning from the river mouth and the beach face to the surf zone. TS1 and TS2 comprise nearly 250 m of the cross-shore domain discretized every 1 m. The frequencies of the ocean waves entering into the lagoon (TS1) and reaching the coast (TS2) are characterized using space-time Hövmoller diagrams. We use two 20-min video segments, recorded between 10:00–10:20 and 10:22–10:42 h, on 2nd August 2023 (the videos are available at Ref. [36]). The total run length spans over 16 800 data points sampled at 7 Hz (40 min). Pixel intensity is normalized using the l^p norm of the RGB vector for each pixel, $(r, g, b) \in [0, 1]^3$, where $p = 10$ provided a clearer visualization of wave fronts. Hanning windows of 4096 data points (∼9.8 min) are averaged with an overlap of 50% to compute the PSD of the normalized pixel intensity time series, from which the frequency distributions of incoming waves along transects can be determined.

To track wave kinematics within the lagoon, we use images captured by a UAV. A DJI Air 2 drone recorded nearly 9 min of a 1920 × 1080 video sampled at 60 Hz, starting at 10:01:50 h on 2nd August 2023 (see the DJI_0001.mp4 file at Ref. [36]). The video is first stabilized using the instantaneous deformation field between consecutive frames following Ref. [50]. Static landmarks are then manually identified. Based on these fixed points, the video is stabilized with respect to their position on the first frame by applying a perspective warp using OpenCV’s warpPerspective function [48]. Then, seven control points are identified in the image frame and manually matched to their respective universal transverse mercator (UTM) coordinates using GoogleEarth Pro, which served as ground truth references. A projective geometric transformation is then fitted using these control points via matlab’s fitgeotrans function, modeling a homography that maps image coordinates to the UTM coordinate system (Fig. 3). The accuracy of the transformation is evaluated by applying the fitted model to the original control points and calculating the Euclidean distance between the transformed points and their known UTM coordinates (see the stabilized and rectified videos available at Ref. [36]). The resulting errors provide a quantitative measure of the transformation’s fidelity, which is on average 6 m, with higher accuracy near the entrance of the lagoon ($\simeq$ 1 m). A transect profile, aligned with the principal direction of incident wave trains, is selected to produce a space-time Hövmoller diagram from the rectified drone video [Fig. 3(b)]. After the projection and interpolation between frames, we obtain a 255-pixel transect distributed over nearly 150 m with an average spacing of $\Delta x \simeq 0.6$ m and temporal resolution of $\Delta t \simeq 0.4$ s. Pixel intensities are normalized as it

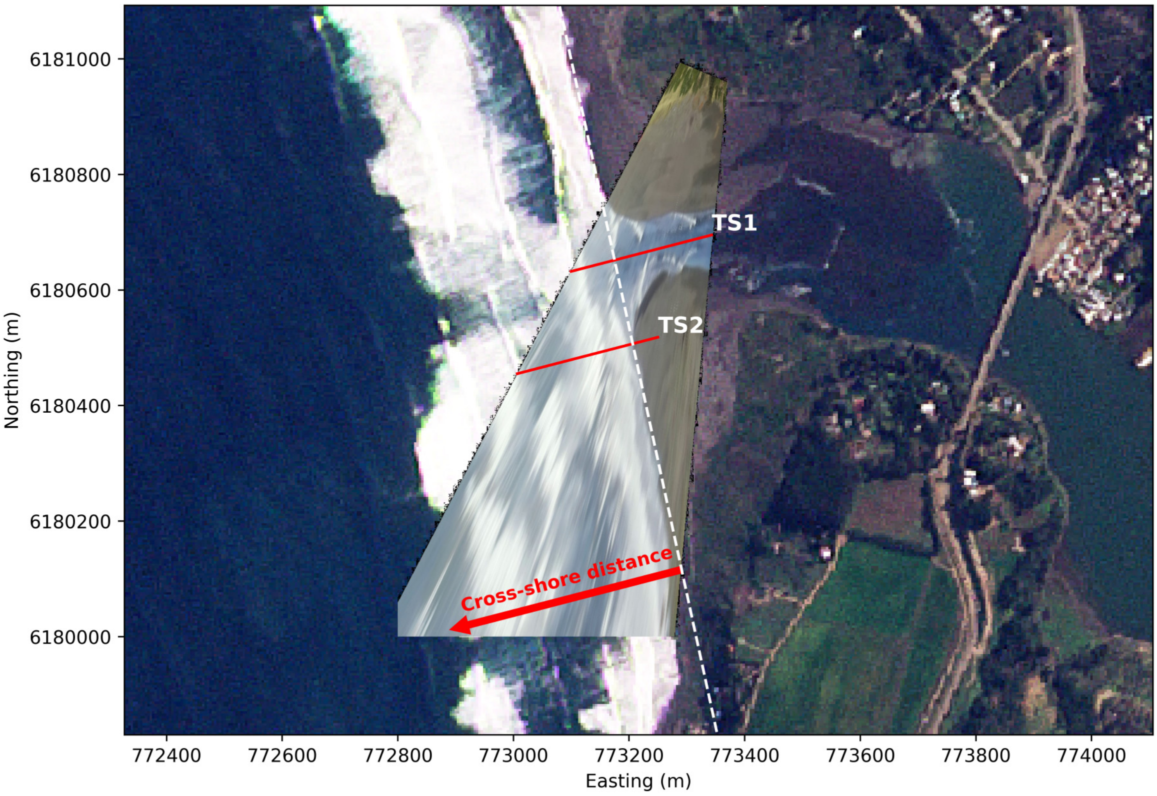

FIG. 2. Georeferenced image frame obtained from the fixed video camera and the location of the transect profiles (TS1 and TS2) to extract space-time Hövmoller diagrams. The background satellite image was taken on 2nd August 2023 [49].

was done with the videos captured by the fixed camera. The obtained wave data are windowed over space-time segments with a Hamming function in both space and time to reduce spectral leakage, and then transformed using a 2D Fourier analysis—fast Fourier transform applied first in time to obtain frequencies, then in space for wave numbers. By applying this technique, the $E(k,\omega)$ spectrum, averaged over windows, can be used to assess the normalized energy distribution across wave numbers and frequencies providing an estimation for the dispersion relation of the observed incident wave trains. Here, $k = 2\pi/L$ is the wave number (L being the wavelength) and $\omega = 2\pi/T$ is the wave angular frequency (T being the wave period).

E. Estimation of the Ursell numbers in the field experiment

We use the definition for the Ursell number given in Ref. [51],

$$U = \frac{3}{16\pi^2}\frac{ac^2T^2}{h^3}, \tag{6}$$

where a and T are, respectively, the wave amplitude and period of the primary long waves, $c = \sqrt{gh}$ is the linear phase velocity, g is the acceleration of gravity, and h is the mean water depth. We note that the inverse of the Ursell number $\epsilon^2 = 1/(2U)$ is used in Ref. [52] to characterize laboratory multisoliton fission regimes from periodic long waves.

The values for the wave amplitude, period, and water depth need to be treated differently compared to laboratory experiments since the field measurements are conducted under uncontrolled conditions. To associate the Ursell numbers with the incident long waves within the IGW frequency band (typically below 0.04 Hz [44]), we apply the zero-up crossing technique [45] to bandpassed water depth signals (Butterworth filter [40] of order 4 with high- and low-pass cutoff frequencies of 0.001 and 0.04 Hz, respectively) to perform the wave-by-wave analysis and identify waveheights and periods. We then estimate a representative Ursell number for each wave gauge station assuming the following:

(1) Representative water depths are estimated averaging the water depth signals over the flood tide of 2nd August 2023.

(2) The long wave amplitude is estimated as $a = H_{\text{IG}}/2$, where H_{IG} is the median of the waveheight distribution of bandpassed signals.

(3) The wave period is estimated as $T = T_{\text{IG}}$, where T_{IG} is the median of the period distribution of bandpassed signals.

F. Numerical experiments with the Serre-Green-Naghdi and KdV equations

To complement the analysis of the field data, we perform a numerical experiment integrating the Serre-Green-Naghdi (SGN) equations using the SERR1D code [53,54] to propagate incident long waves with amplitudes and frequencies compatible with the ones entering into Laguna Cáhuil. The wave field is propagated from the ocean border of the lagoon (absorbing-generating left boundary condition [55]) into the measured bathymetric profile shown in Fig. 4, considering a moving shoreline boundary condition on the eastern

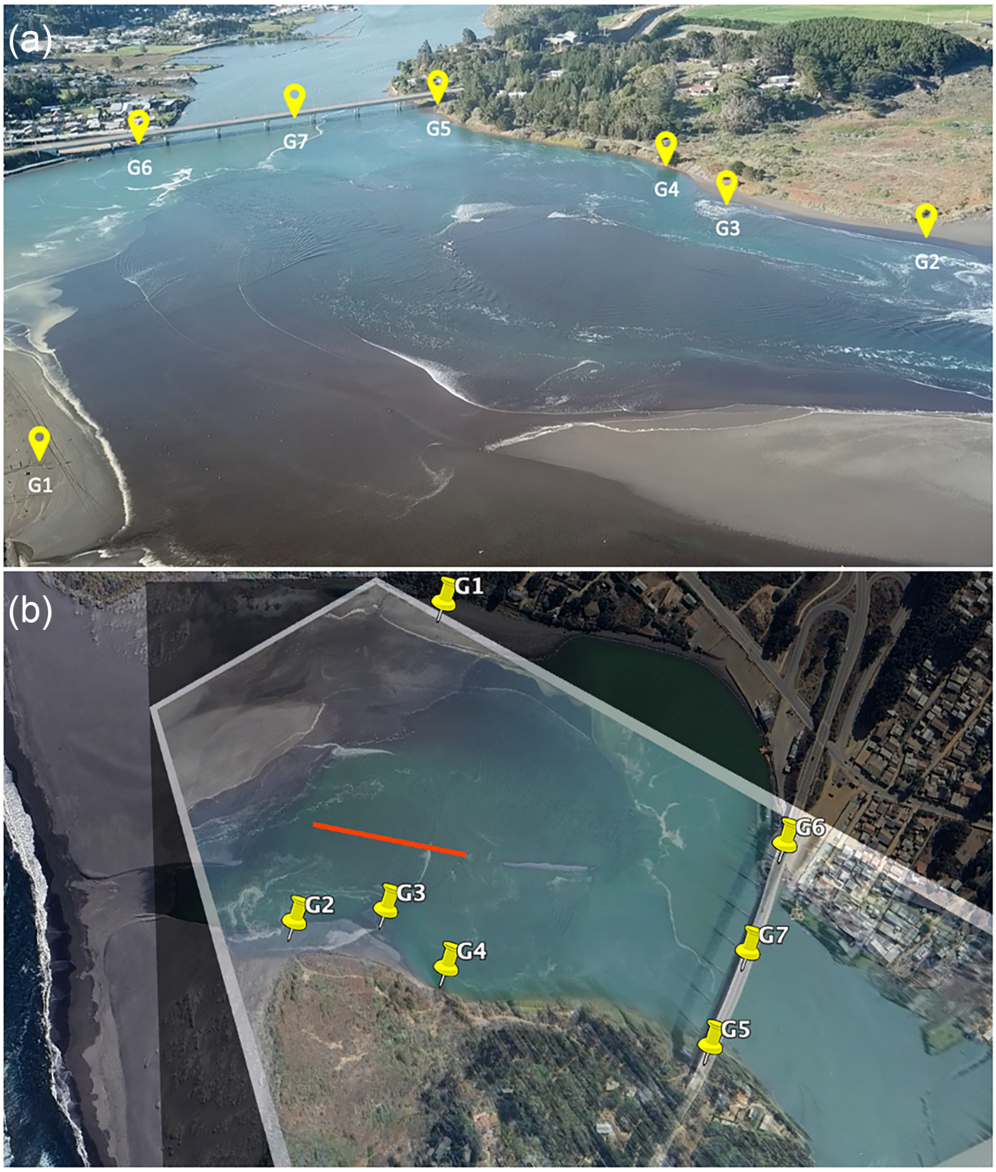

FIG. 3. Rectification process for the video captured by the UAV. (a) Identification of georeferenced points in the original image. (b) Projection of the original image into a georeferenced Google Earth Pro satellite image. The red line depicts the transect profile used to produce the space-time Hövmoller diagram from the rectified video.

border (right), where incoming waves can reflect. The numerical integration is performed taking spatial and temporal discretizations of $\Delta x = 0.3$ m and $\Delta t = 0.0782$ s for a total duration of 23 400 s, using a constant Manning friction factor $n = 0.025$.

Numerical experiments are also performed using the KdV equations using the numerical implementation described in Ref. [56]. The propagation of periodic waves with characteristics compatible with the measured incident long waves is conducted on an idealized channel of constant depth, using a fourth-order Runge-Kutta scheme in time, splitting the linear and nonlinear terms with a fractional stepping method, and using a fast-Fourier-transform-based spectral method in space. The numerical solver is run using spatial and temporal discretizations of $\Delta x = 0.000\,66$ m and $\Delta t = 0.029$ s, but are subsampled in space to $\Delta x = 0.6641$ m for the analysis presented below.

G. Nonlinear Fourier analysis of wave signals

Nonlinear Fourier transforms enable the detection of potentially hidden solitons in time or space series [8,57]. In particular, they can provide the amplitudes and phases of each soliton. With this information, one can compute the so-called *soliton energy ratio* [58]. This is a number between zero and one, where zero means that there are no solitons at all and one means that the signal consists only of solitons. The soliton energy ratio is based on nonlinear versions of Parsevals relation, by which the "energy" E of a time series $\eta(t)$ satisfies

$$E = \int_{-\infty}^{\infty} |\eta(t)|^2 dt = E_{\text{soliton}} + E_{\text{continuous}},$$

where $E_{\text{soliton}} \geqslant 0$ is computed from the solitonic part of the nonlinear Fourier spectrum and $E_{\text{continuous}} \geqslant 0$ is computed

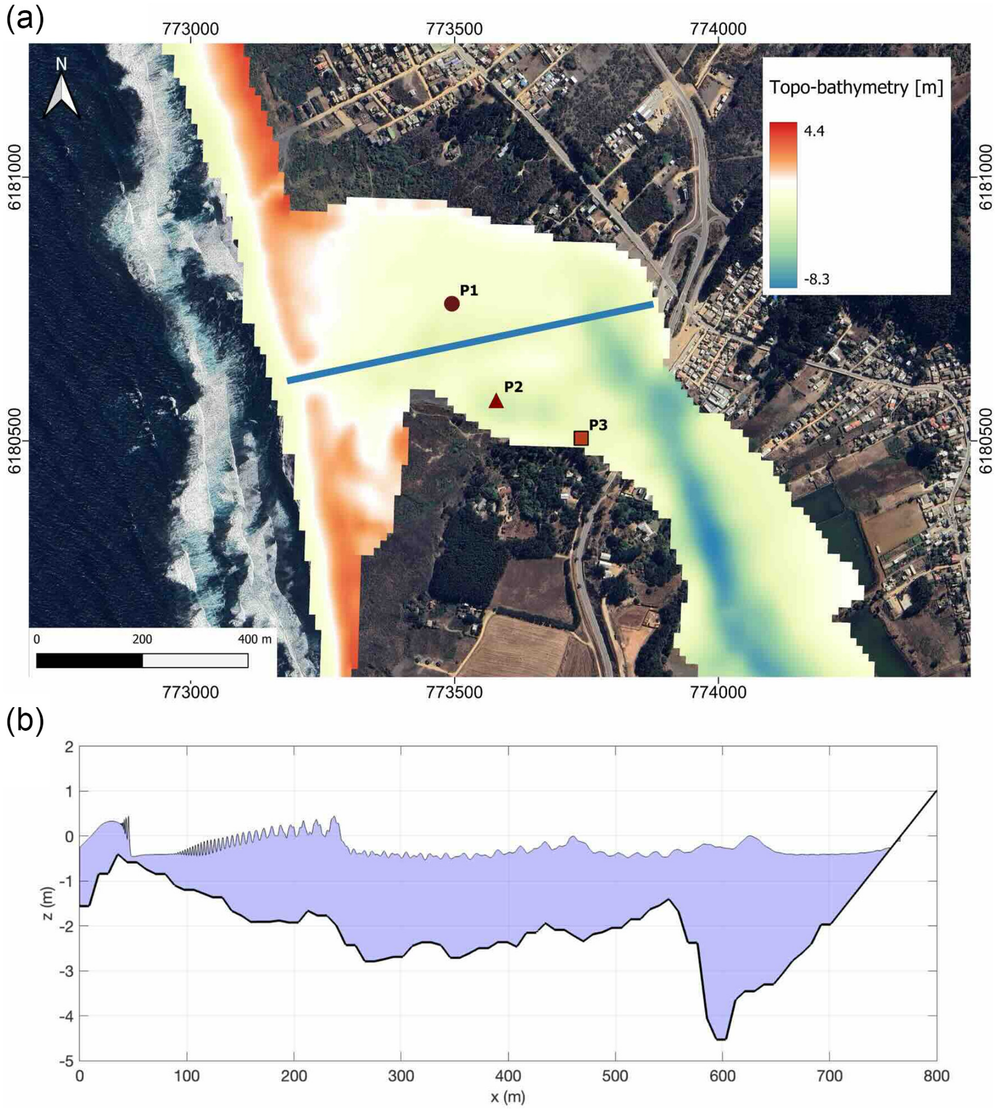

FIG. 4. Profile transect used for the numerical experiment using the Serre-Green-Naghdi equations. (a) Topobathymetry of the Laguna Cáhuil (measured between 24 and 27 March 2023) and the selected transect for the simulations (blue line). The locations of the instruments moored during the field campaign are shown in colored symbols. (b) Snapshot of the simulation and bathymetric profile (the free surface time series are multiplied by a factor of 5 to facilitate the visual inspection).

from the nonsolitonic part of the NFT. The soliton energy ratio is given by E_{soliton}/E.

Different kinds of NFTs exist for different types of propagation models. Here, we consider the NFT for the vanishing KdV equation [8,59]. The KdV is a weakly nonlinear and weakly dispersive shallow water equation. The time series considered below greatly satisfy the main applicability condition, i.e., $kh \ll 1$, where k is the dominant wave number and h is the reference water depth.

To compute the KdV-NFT numerically, we employ the development version of the software library FNFT (commit 6d1c36b92) [60] with vanishing boundary conditions. The underlying algorithm is a simplified version of the method described in Ref. [61]. The accounting function is computed as described there for the second-order case. Then, bisection is used to bracket the eigenvalues. Intermediate results of the scattering process are rescaled to avoid the range of floating point numbers being left occasionally. The formulas required to compute the soliton energy ratio for the KdV case are provided, e.g., in Eq. (23) of Ref. [62].

III. ANALYSIS OF THE RECORDED WAVE FIELD

Water depth measurements are reconstructed from bottom-moored pressure signals following Ref. [37] as described in Sec. II B. Measured time series and associated spectrograms are shown in Fig. 5; the highest energy content belongs to tidal modulations at longer periods (>128 min). Significant patches of wave energy are also visible within the IGW frequency band (typically defined between 0.42 and 4.2 min [44]), only during the flood tides. Hereafter, we analyze the time series during the flood tide of 2nd August, which was the largest captured by all the instruments (depicted in the red boxes shown in Fig. 5).

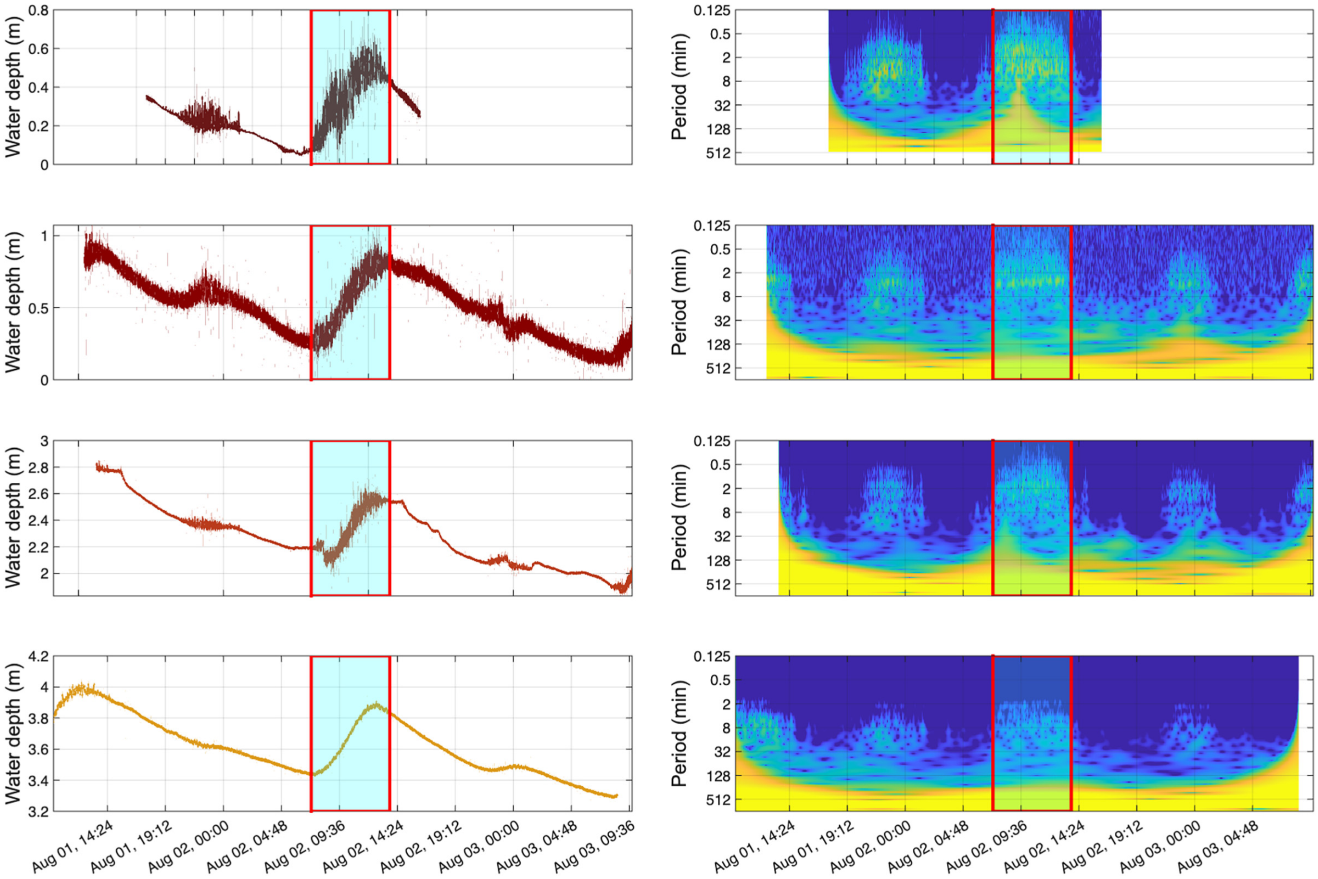

FIG. 5. Reconstructed water depths from the bottom-moored pressure signals recorded at the locations shown in Fig. 1. Left panel: Recorded time series (color key: P1 ▬, P2 ▬, P3 ▬, P4 ▬). Right panel: Normalized spectrograms of the signals. The flood tide segment used to analyze the spectral and statistical characteristics of the wave field is shown in red boxes.

A. Measured wave field and associated spectrograms

Time series are high-pass filtered with a cutoff frequency of 0.001 Hz (16 min) to damp out longer-period oscillations associated with tidal modulations, enabling the analysis of the recorded signals within the sea-swell-IGW frequency band (see Sec. II B). The filtered time series during the flood tide of 2nd August and their spectrograms are presented in Fig. 6. The spectrograms show a broad energy content within the IGW frequency band (periods above 0.42 min) with no clear frequency dominance and a downshift in frequency for P4 located nearly 3 km upstream the river mouth. A similar frequency downshift was observed for IGWs propagating upstream a similar bar-built estuary in Ref. [63].

The recorded time series, normalized with respect to the average of the highest third of waveheights in the background signal, $H_{1/3}$, are shown in the left panel of Fig. 6. The presence of rogue waves is evidenced in all gauges using the crest height criterion threshold $\eta_c/H_{1/3} > 1.25$ [64,65]. To confirm and quantify these, statistical and spectral properties of the recorded time series are presented in the next section.

B. Waveheight distributions, high-order moments, and spectral properties of the measured wave field

To characterize the statistical properties of the free surface signals and quantify the presence of rogue waves, individual waves are isolated using the zero-up crossing method (see Sec. II C). Several rogue waves measured at P3 can be inspected in the 2-h segment shown in Fig. 7(a). In Figs. 7(b) and 7(c), we show the waveheight, $P(H/H_{1/3} > x)$, and crest height, $P(\eta_c/H_{1/3} > x)$, empirical exceedance probabilities. All the measured signals lie consistently above the distribution that characterizes a Gaussian random wave field, and the presence of rogue waves is confirmed also from the waveheight threshold criterion $H/H_{1/3} > 2.2$ [64,65]. The probability of encountering a rogue wave considering $P(H/H_{1/3} > 2.2)$ or $P(\eta_c/H_{1/3} > 1.25)$ is several orders of magnitude higher than that for linear wave superposition.

High-order moments of measured free surface time series can provide additional insights into the wave field characteristics and are presented in Fig. 8. Wave left-right asymmetry (As) and wave skewness (Sk) show distinct evolution between gauges. Near the entrance of the lagoon at P1, waves are highly asymmetric as As $\simeq -0.6$, an indication of nearly breaking conditions; within the lagoon (P2 and P3), the asymmetry tends to decrease, while for P4, left-right asymmetry is mild (As $\simeq 0.05$) suggesting that nonlinear and dispersive effects equilibrate as long waves propagated over nearly 3 km upstream in the river channel. Skewness increases steadily from one station to the next, reaching a maximum Sk $\simeq 0.34$ at P3. For P4, the skewness value is small and positive (Sk $\simeq 0.03$). The kurtosis values for the instruments moored

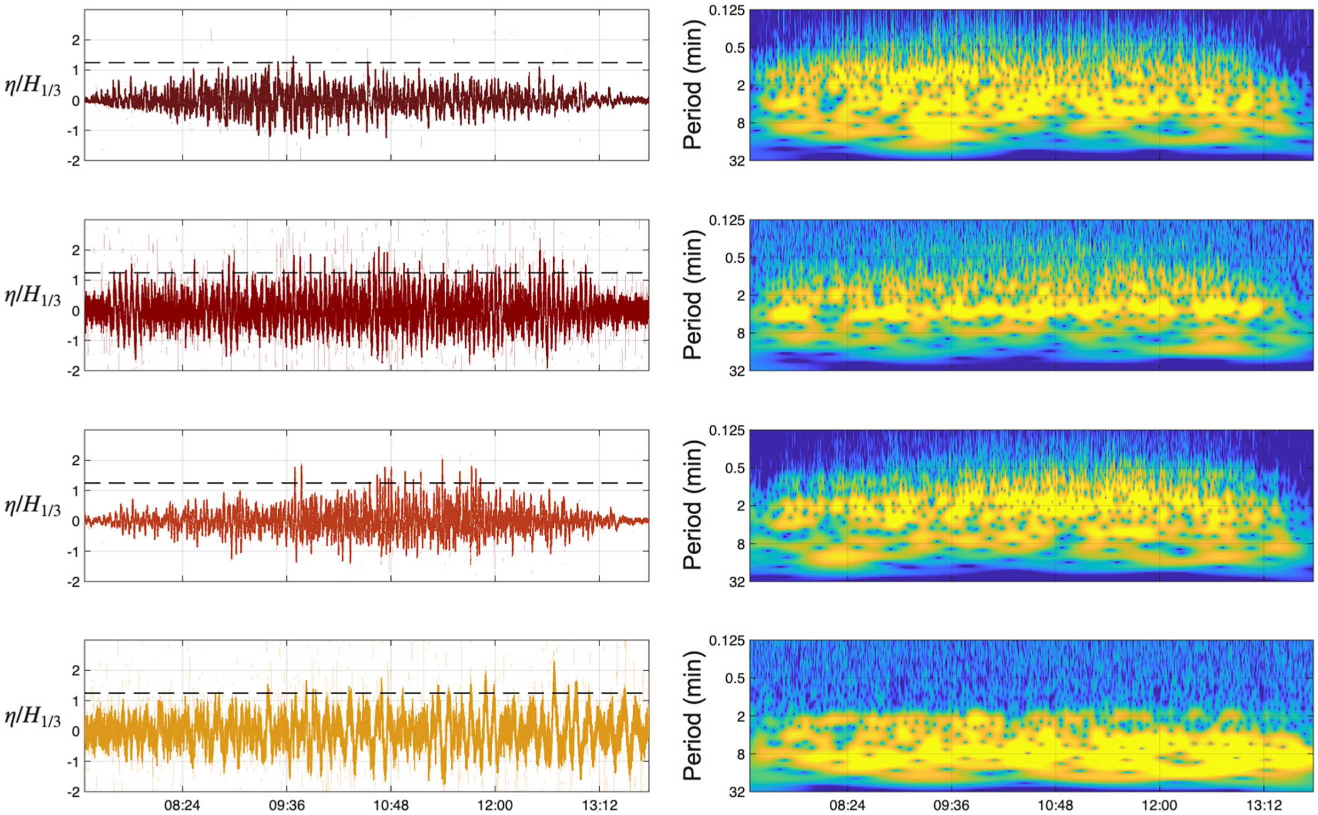

FIG. 6. High-pass filtered (cutoff frequency of 0.001 Hz) signals of the water depth records at the locations shown in Fig. 1 for the flood tide of 2nd August 2023. Left panel: Recorded time series and rogue wave threshold ($\eta_c/H_{1/3} = 1.25$) depicted in a dashed black line (color key: P1 ▬, P2 ▬, P3 ▬, P4 ▬). Right panel: Normalized spectrograms of the time series.

within the lagoon (P1–P3) are all above Ku = 3 that characterizes a Gaussian process (with Ku $\simeq$ 4.6 at P3), confirming the strongly non-Gaussian nature of the wave field there. At P4, the kurtosis value is smaller but still remains slightly above 3 (Ku $\simeq$ 3.1).

The PSD of the free surface signals is shown in Fig. 7(d). The spectra of the three instruments moored closer to the river mouth (P1–P3) show a nearly exponential decay within the IGW frequency band (0.004–0.04 Hz); for higher frequencies, the energy decay tends to follow a power law (between f^{-1} and f^{-2}). Rather flat spectra are observed for shorter wavelengths ($f > 0.1$) at stations P2 and P3, evidencing the randomization of the wave field for shorter wavelengths. A strong damping of frequencies above 0.01 Hz is observed at P4 located far upstream, but an increase in energy is clearly visible for higher frequencies ($f > 0.1$ Hz), hence suggesting an energy transfer from long to shorter wavelengths during the propagation of long waves upstream the river channel.

C. Evidence of soliton gas dynamics within Laguna Cáhuil

The observed waveheight distributions with a probability of encountering rogue waves several orders of magnitude higher than that for linear wave superposition are consistent with those reported in numerical and laboratory experiments as SG dynamics [23,24,28,31,51]. In addition, similar high kurtosis values have been obtained for the SG generated in a wave flume by Redor *et al.* [51]; moreover, a value of Ku = 4 has been theoretically shown to correspond to a stationary limit of SG dynamics developing from narrow-band partially coherent waves resulting in a 1.5 orders of magnitude increase in the probability of encountering rogue waves compared to the linear theory in an integrable turbulence framework [30]. This value is reached at locations P1 and P3. Skewness shows an evolution with negative curvature, which peaks at sensor P3 within the lagoon. Similar evolution patterns of Sk were reported in a solitonic gas by Dutykh and Pelinovsky [66] from direct numerical simulations conducted with a nonintegrable KdV set of partial differential equations.

The exponential signature decay close to the forcing frequency shown in the instruments moored within the lagoon (P1–P3) is a characteristic of SG obtained in numerical simulations [20,67], measured in optical experiments [28,29], and in a bidirectional laboratory wave flume [17,51]. The power-law decay is consistent with the ones reported in the field observations of Costa *et al.* [12] as soliton turbulence.

To confirm the presence of solitons in the measured time series, we apply the KdV-NFT algorithm (see Sec. II G) to the 2-h segment measured at P3 shown in Fig. 7(a). The KdV-NFT algorithm assumes a flat bottom and unidirectional propagation, which is why it can describe the investigated dynamics only approximately. In particular, the unidirectionality assumption might be critical for the measured data since incident and reflected waves can propagate in multiple directions within the lagoon. Despite these limitations, the NFT is useful to detect the presence of solitons in the measured time series.

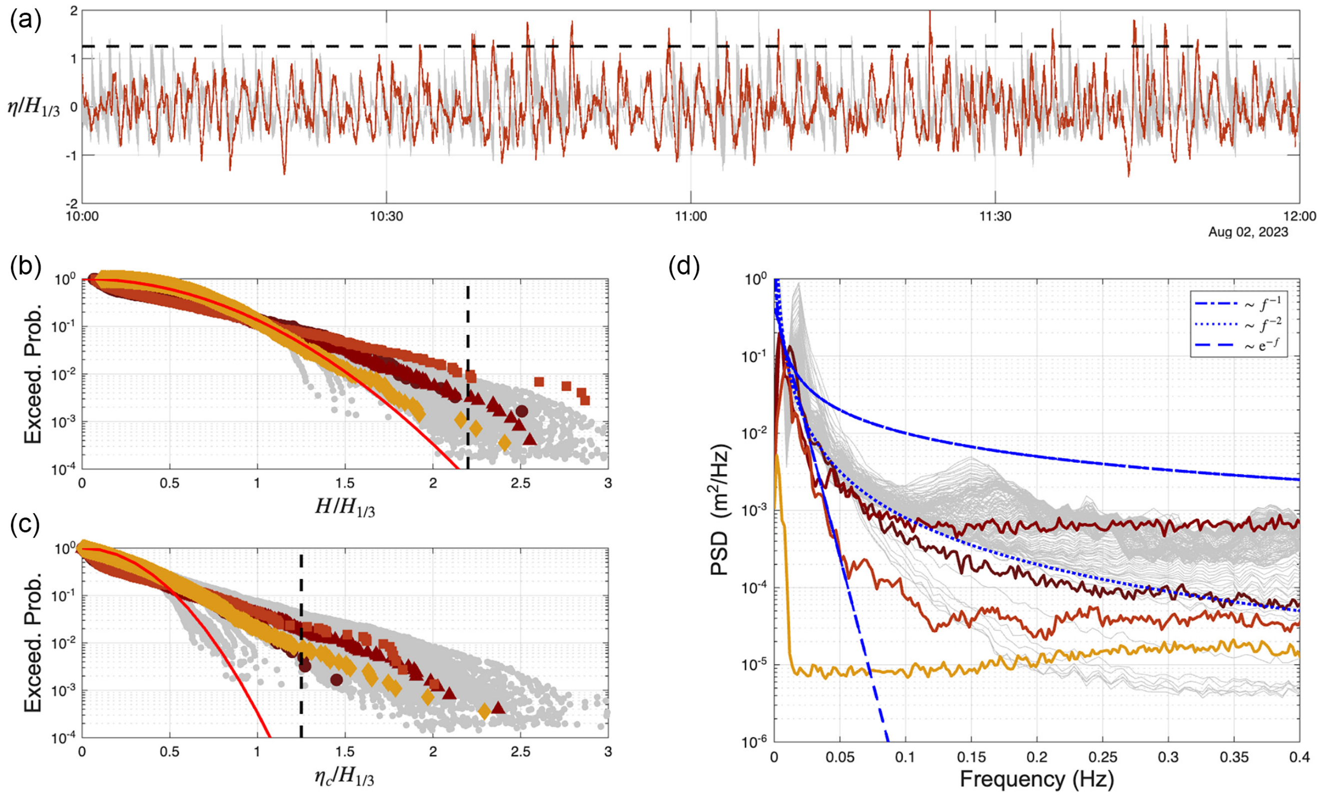

FIG. 7. Statistical and spectral properties of free surface signals during the flood tide of 2nd August 2023. (a) Two-hour segment of the normalized time series recorded at location P3. (b) Waveheight empirical exceedance probability. (c) Crest height empirical exceedance probability. The distributions associated with a Gaussian wave field are plotted in red solid lines as reference and the black dashed lines show the threshold criteria for rogue waves. (d) Power spectral density of the time series. Color key: P1 ●, P2 ▲, P3 ■, P4 ♦. In the background of each graph, we show the results from the SGN numerical experiment in light gray [the time series shown in panel (a) is extracted from a virtual gauge located at $x = 200$ m; see Fig. 4].

For the time series sampled at 1 Hz with a mean water depth of 2.35 m (see Table II), the KdV-NFT detects 287 solitons with amplitudes ranging from 21.56 cm down to 0.02 cm. The complete distribution of soliton amplitudes is provided in Fig. 9. The resulting soliton energy ratio is 0.53, which means that the signal is dominated by KdV-type soliton dynamics.

So far, our results are indicative of an SG dynamics resulting in a strongly nonlinear wave field attaining a statistically quasistationary state within the lagoon, as similar PSDs, exceedance probability distributions, and stable kurtosis values are observed at different locations there (P1–P3). To confirm this, we need to identify the soliton release mechanism from the transformations that incident ocean swells undergo

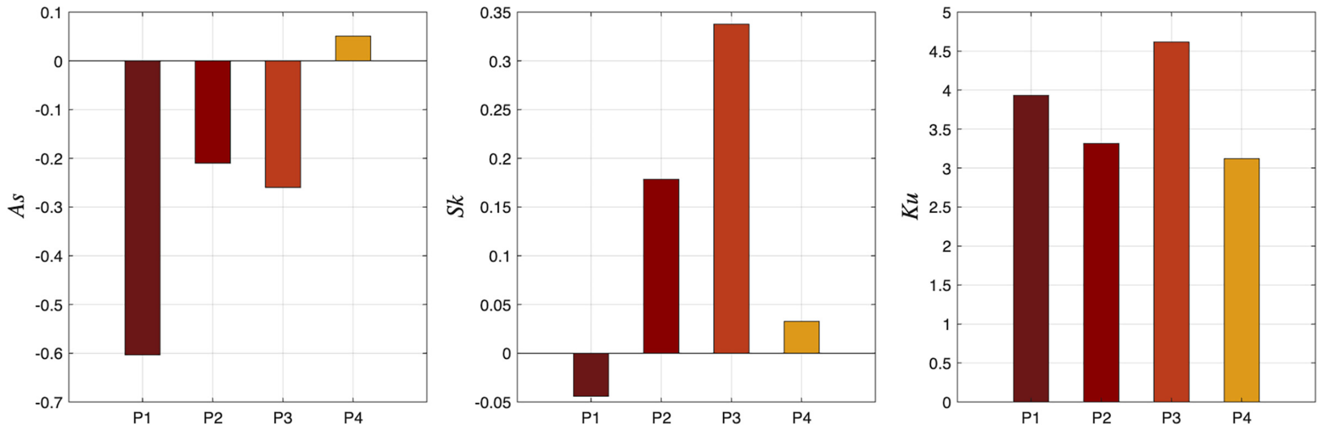

FIG. 8. High-order moments of measured free surface time series. Left panel: Asymmetry (As). Central panel: Skewness (Sk). Right panel: Kurtosis (Ku).

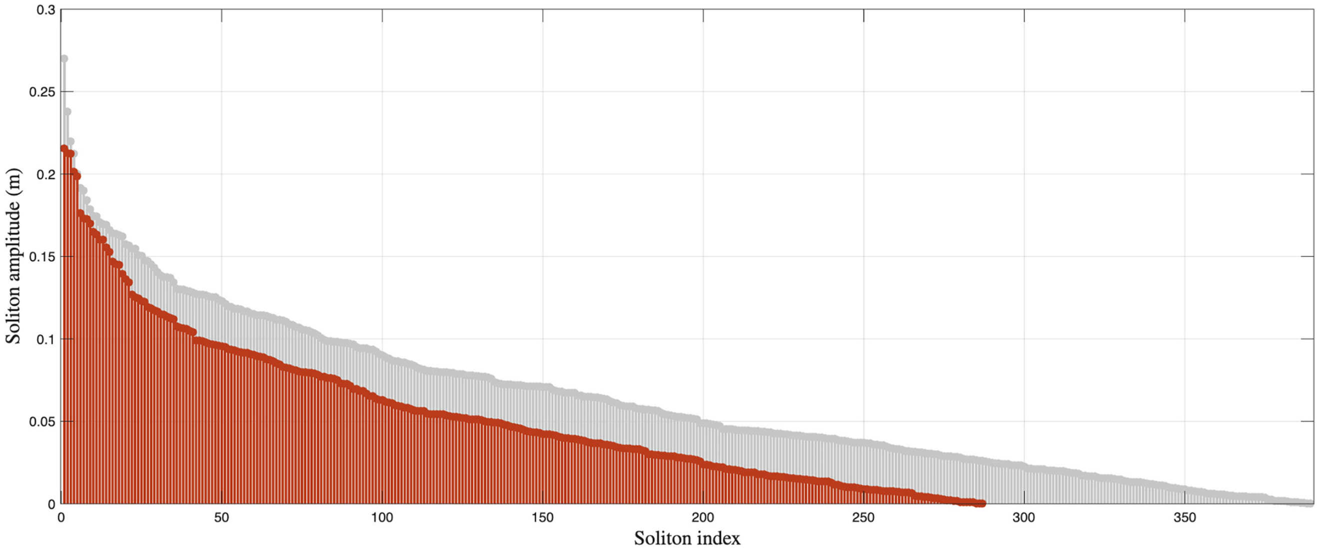

FIG. 9. Soliton amplitudes for the 2-h segment recorded at P3 [see Fig. 7(a)] computed using the NFT-KdV algorithm. In the background, the soliton amplitudes resulting from the application of the NFT-KdV to the SGN numerical experiment are shown in light gray [the analyzed time series is shown in light gray in Fig. 7(a)].

when reaching the coast and penetrate Laguna Cáhuil. For this purpose, incident wave kinematics are studied in the next section.

D. Multisoliton fission from incident infragravity waves entering into Laguna Cáhuil

Ocean waves reaching the coast and propagating into the bar-built estuary during the flood tide of 2nd August were captured by a fixed high-resolution video monitoring system (see Sec. II D). The incident wave frequencies are characterized from a 40-min record starting at 10:00 h using space-time Hövmoller diagrams of optical pixel intensity over two cross-shore transects (TS1 and TS2 in Fig. 2; Hövmoller diagrams are shown in the left panel of Fig. 10). In the right panel of Fig. 10, the PSDs computed from the normalized pixel intensities along transects (see Sec. II D) clearly show the peak period of the incoming swells ($\simeq 13.4$ s), while over the beach transect (TS2), break-point modulations at IGW frequencies show a strong surf-beat forcing as described in Refs. [68,69]. Along the river mouth channel (TS1), it is seen that the swell energy is strongly damped, and only long waves in the IGW frequency band penetrate into the lagoon. This is in agreement with the low-pass filtering effects observed in similar configurations from field measurements [63,70] and from numerical experiments using the fully nonlinear and weakly dispersive SGN equations [54].

TABLE II. Ursell numbers for primary long waves at each station based on the estimated characteristic values for the relevant variables (see Sec. II E).

Station	h (m)	a (m)	T (s)	U	ϵ^2
P1	0.36	0.049	84.0	511.7	0.0010
P2	0.56	0.036	98.0	203.3	0.0025
P3	2.35	0.031	92.0	8.8	0.0568
P4	3.68	0.004	194.5	2.0	0.2525

IGWs thus breach the bar sporadically and propagate upstream the river mouth over a shallow and gradually varying bathymetry. We compute the Ursell numbers associated with the IGW signals recorded at the different pressure sensors as described in Sec. II E. The estimated Ursell numbers close to the entrance of the lagoon at P1 and P2 are on the order $U \sim 100$ (see Table II), hence comparable with the ones leading to multisoliton fission from periodic long waves in the laboratory experiments of Trillo *et al.* [52].

The kinematics of IGWs entering into the lagoon can be further studied using the video captured by a UAV as described in Sec. II D. The wave field is analyzed along a transect representing the main direction of propagation of observed incoming wave trains [see Fig. 3(b)]. In Fig. 11, the resulting space-time Hövmoller diagram is shown, where eight incident long wave trains are accurately captured, penetrating into the lagoon at temporal intervals between 40 and 200 s, thus compatible with the IGW frequencies observed in Fig. 10(a). Following Ref. [17], we apply the space-time Fourier transform as described in Sec. II D to obtain the 2D spectrum averaged over the eight x–t windows shown in Fig. 11. The resulting $E(k,\omega)$ spectrum shown in Fig. 12 demonstrates that the kinematics of incident long wave trains correspond to solitons since the strongest energy level of forward propagating waves ($k > 0$) is a straight line in the k–ω space (the linear dispersion relation is plotted in white curves as reference). We obtain $c = \omega/k \simeq 4.1$ m/s, giving a referential water depth $h \simeq 1.7$ m using the linear long wave celerity. Energy associated with back-traveling waves ($k < 0$) is also visible in Fig. 12, but its interpretation is more complex since reflected waves could propagate in different directions.

Hence, long IGWs penetrating into the lagoon fission into solitons as the Ursell numbers computed for P1 and P2 in Table II suggested. To further confirm this, we run the periodic KdV model described in Ref. [56] using parameter values $a = 0.2$ m, $T = 60$ s, and $h = 1.7$ m, on the order of the incident IGW field observed within the lagoon. The KdV model

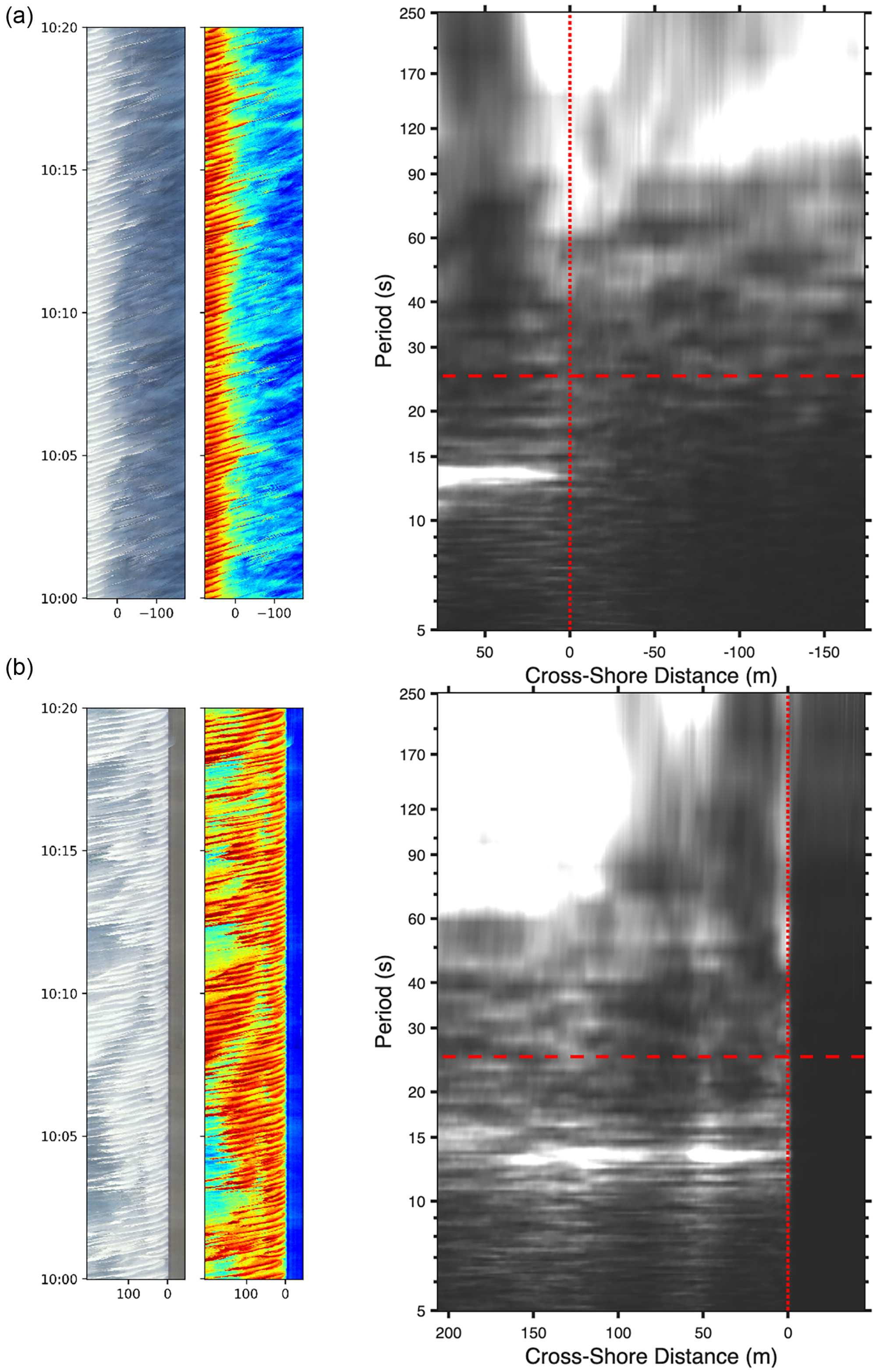

FIG. 10. Remote sensing of the incident ocean swells and infragravity wave motions during the tidal flood of 2nd August 2023 for transects TS1 (a) and TS2 (b) shown in Fig. 2. Left panels: Hövmoller diagrams for raw space-time RGB time series and using the pixel intensity normalization described in Sec. II D. Right panels: Cross-shore evolution of wave frequencies along transects. The horizontal and vertical dashed red lines show, respectively, the limit between swell and infragravity frequency bands, and the shoreline position.

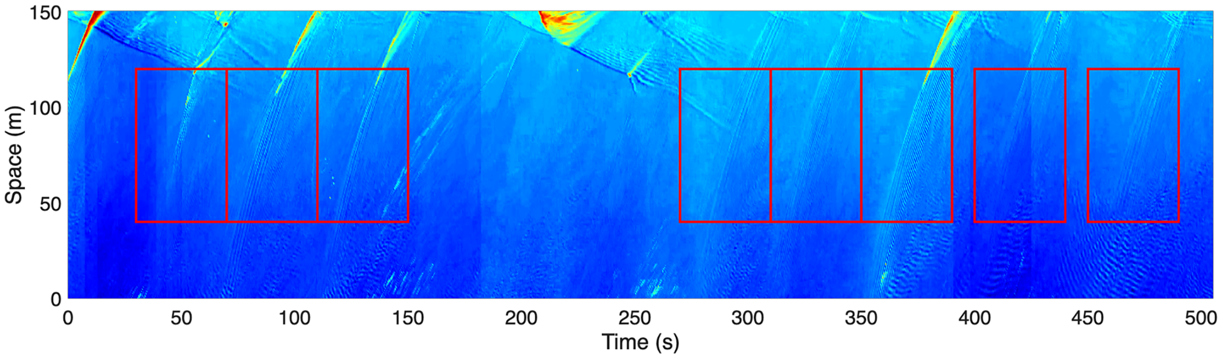

FIG. 11. Space-time Hövmoller diagram for the transect profile obtained from the UAV video [see Fig. 3(b)] showing the kinematics of infragravity waves penetrating into Laguna Cáhuil. RGB time series are normalized as described in Sec. II D. Detected incident long wave trains are depicted within x–t red windows.

produces a multisoliton fission of the primary long waves (see the snapshot in the upper panel of Fig. 13) resulting in an $E(k,\omega)$ spectrum consistent with the one obtained from the UAV video as shown in the lower panel of Fig. 13. It is thus demonstrated that solitons are released from the fission of incident IGWs while entering into the lagoon, a mechanism that was first described by Zabusky and Kruskal [2].

IV. FROM OCEAN SWELLS TO SOLITON GAS DYNAMICS IN A NATURAL COASTAL ENVIRONMENT

The path to the SG regime in our field experiment is now conceptualized. Swells are long-lived narrow-band wind waves at frequencies between 0.04 and 1 Hz that propagate over thousands of kilometers across the world's oceans carrying most of the global surface wave energy [71]. While approaching the coast, IGWs with typical frequencies between 0.004 and 0.04 Hz are enhanced by nonlinear shallow water processes that transfer energy from the swell frequencies to the IGW frequency band [44]. Within the surf and swash zones, IGWs can be released by the breaking of their short-wave parents and then propagate as free long waves [43]. Recent field observations [63,70] and a numerical simulation using a fully nonlinear and weakly dispersive shallow water wave model based on the SGN equations [54] have shown that IGWs generated from surf-zone processes and released by breaking can penetrate shallow bar-built estuaries and propagate long distances upstream. In the surf zone and at the river mouth, the wave energy in the swell frequency band is completely damped and IGWs are released as free

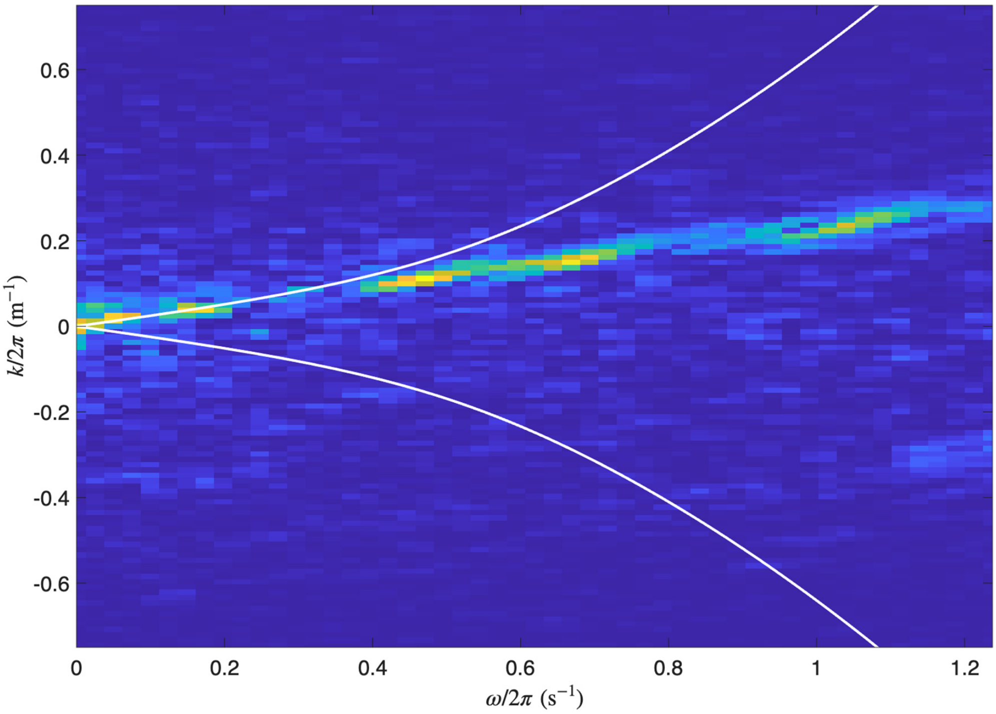

FIG. 12. Normalized $E(k,\omega)$ spectrum of the measured incident wave field averaged over the x–t windows shown in Fig. 11. The linear dispersion relation using a water depth $h = 1.7$ m is shown in the white curves as reference.

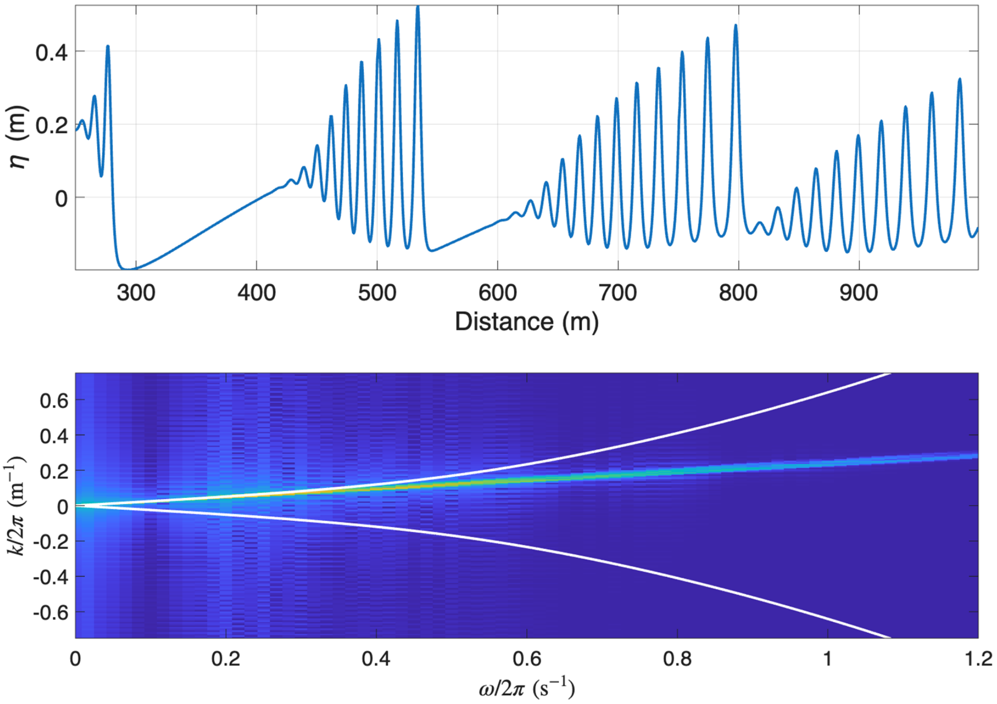

FIG. 13. Kinematics of the KdV multisoliton fission from a sinusoidal wave with amplitude $a = 0.2$ m, period $T = 60$ s, and reference water depth $h = 1.7$ m. Upper panel: Snapshot of the modeled free surface. Lower panel: Normalized $E(k, \omega)$ spectrum of the free surface time series. The linear dispersion relation using a water depth $h = 1.7$ m is shown in the white curves as reference.

long waves, propagating upstream into the estuary and river channel during flood tides, when subcritical conditions are enhanced [54,63,70]. Hence, shallow river mouth configurations can operate as a natural low-pass filter allowing to directly track the fate of IGW motions.

At Laguna Cáhuil, surf-zone-generated IGWs provide the energy input for the formation and development of the SG regime. As schematized in Fig. 14, the river mouth is exposed to energetic ocean swells (Fig. 14, inset A) that enhance the generation of IGWs within the surf zone. IGWs breach the bar sporadically and propagate upstream the river mouth where they experience multisoliton fission (Fig. 14, inset B). The continuous injection of soliton trains that propagate within the lagoon over a shallow and gradually varying bathymetry leads to refraction and reflections enhancing intense wave-wave interactions (see Fig. 14, insets D and E, and Fig. 15). The repeated interactions between solitonic waves shall explain reaching the measured quasistationary wave field compatible with an SG regime. To test this hypothesis, we conduct numerical simulations over a transect profile of Laguna Cáhuil using the SGN model described in Refs. [53,54] (see Sec. II F). The SGN equations are nonintegrable in the strict sense, but admit at least four conservation laws and closed-form solutions for cnoidal and solitary waves over horizontal bottoms [72], and can produce dispersive shock waves [73,74].

In the numerical experiment, the incident IGW field is built from a narrow-band JONSWAP spectrum with significant spectral waveheight $H_{m0} = 0.2$ m, peak period $T_P = 60$ s, peak enhancement factor $\gamma = 3.3$, and a random phase distribution between the harmonic components [75], to qualitatively comply with the measured one. This wave field is propagated from the ocean border of the lagoon as described in Sec. II F. We compute the statistical and spectral properties for the numerical time series in virtual gauges spaced every 5 m between $x = 0$ and $x = 750$ m (see Fig. 16) applying the same methods described for the measured water depths, discarding the first 1800 s of the simulations (warming up of the model). A 2-h free surface time series extracted from a virtual wave gauge located at $x = 200$ m is shown in light gray in Fig. 7(a), where similar wave patterns compared with the field measurements are observed, including the frequent appearance of rogue waves. The location of the virtual wave gauge in the simulation ($x = 200$ m in Fig. 16) is chosen inside the lagoon with a similar mean water depth as location P3 for the field experiment.

In the numerical experiment, "new" and "old" solitons interact continuously (see the animation available at Ref. [36]) resulting in statistical and spectral properties showing striking resemblances with the ones measured within Laguna Cáhuil (Figs. 7 and 16), hence supporting our conjectures. It is worth noting that in the SGN experiment, the significant waveheights and the high-order moments of the time series show mild spatial variations over a large portion of the lagoon profile. In particular, the kurtosis reaches an almost constant value, Ku = 4, between $x = 100$ m and $x = 320$ m, hence suggesting that a quasistationary wave field is reached there.

We also apply the KdV-NFT algorithm to the 2-h time series segment obtained from the SGN simulations shown in light gray in Fig. 7(a). The numerical time series is resampled (linear interpolation between points) at $1/0.1048 \approx 9.54$ Hz, and the mean water depth at the virtual gauge is estimated to be 1.83 m. The KdV-NFT detects 389 solitons with

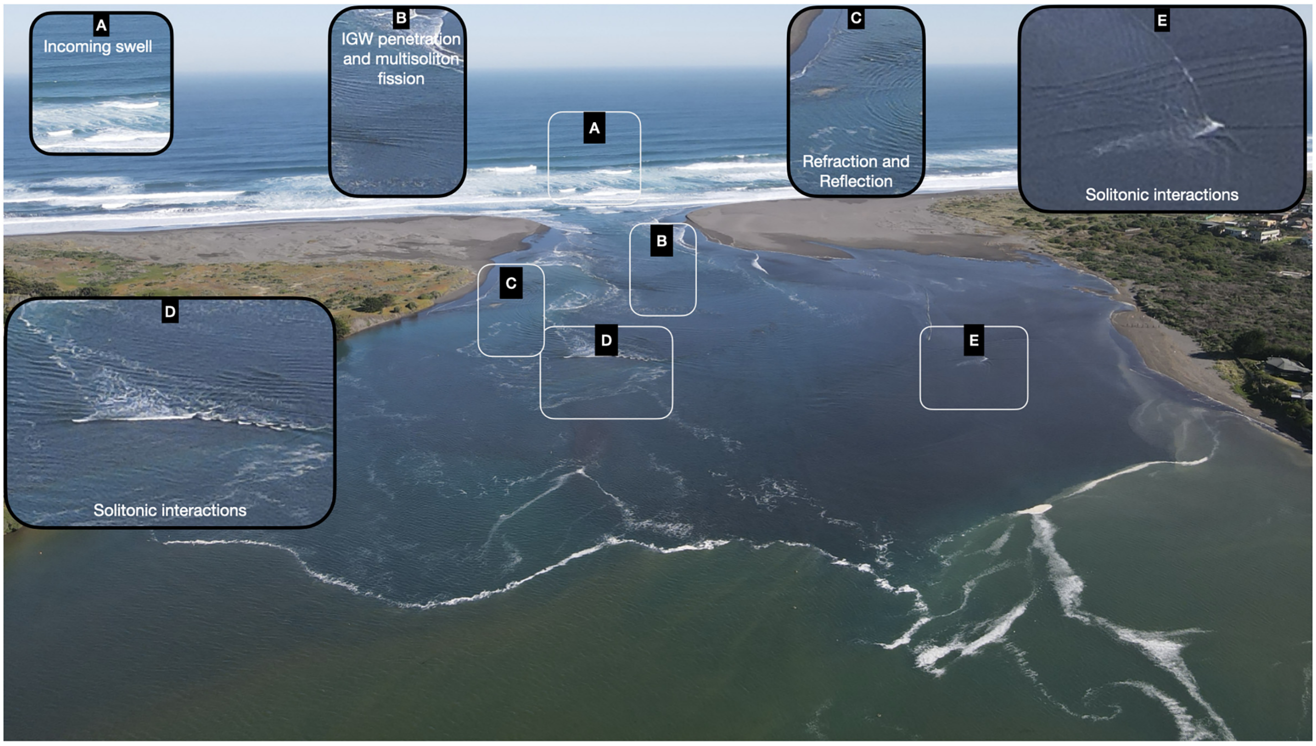

FIG. 14. Snapshot of the wave field during the field experiment where most instances of the conceptual model for the generation of the soliton gas regime at Laguna Cáhuil can be observed. Callouts refer to enlarged inset images. Explanations are provided in the main text.

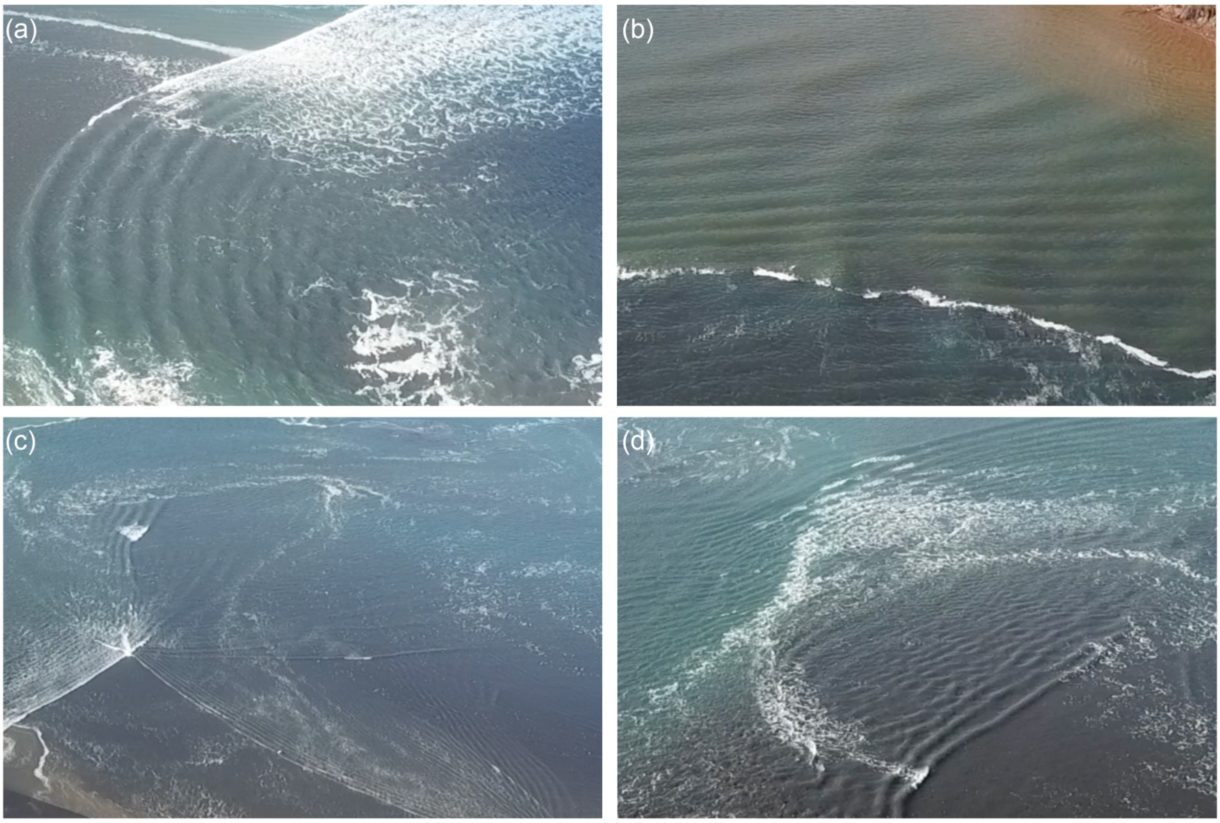

FIG. 15. Solitonic interactions after the penetration of infragravity wave motions in Laguna Cáhuil during the flood tide of 1st August 2023, 10:10 h. Images captured by an unmanned aerial vehicle. (a) Dispersive shock waves and multisoliton fission and refraction over shoals. (b) Cross-propagating solitonic wave fields. (c) X- and Y-type shallow water solitons emerging from oblique crossings in very shallow waters. (d) A solitonic wave train propagating toward the river mouth after reflecting at the lagoon borders, while another solitonic wave train propagates upstream.

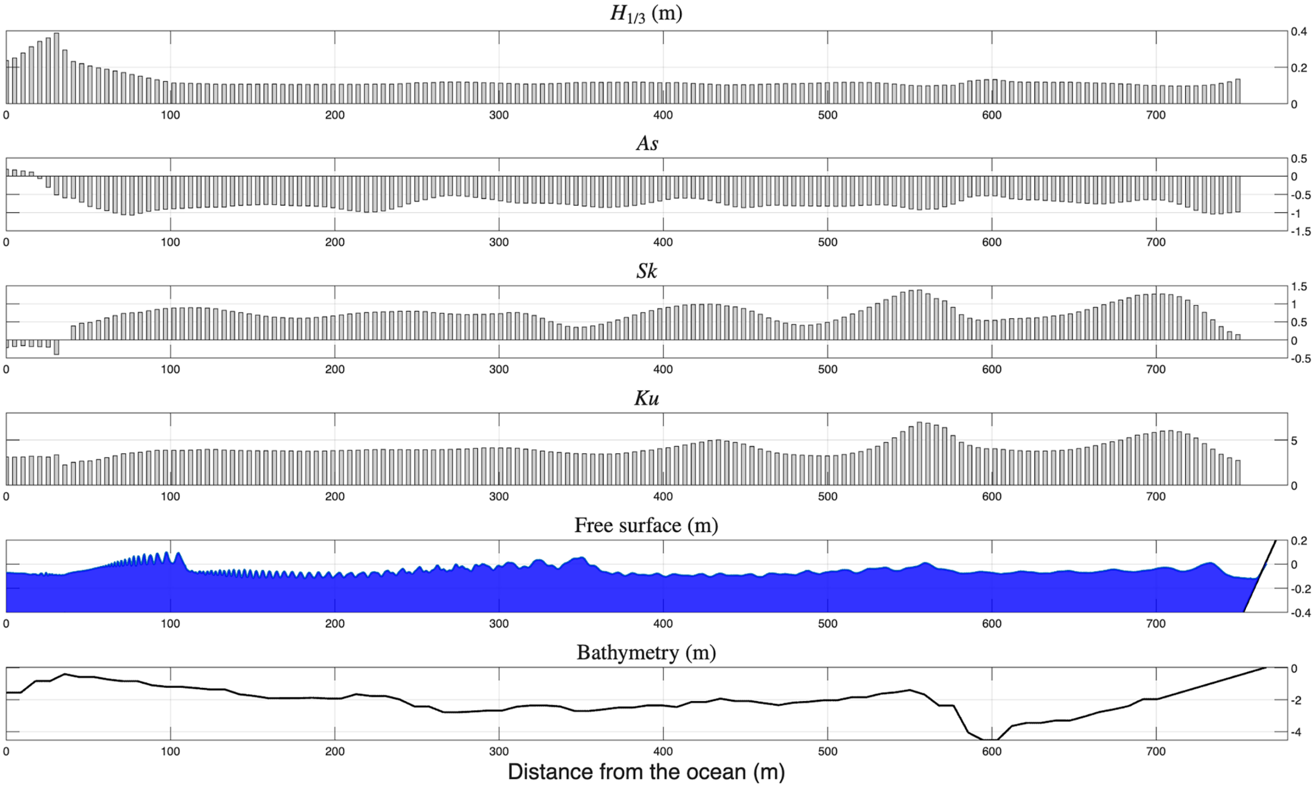

FIG. 16. Results obtained from the numerical experiment using the Serre-Green-Naghdi equations. From top to bottom: significant waveheights ($H_{1/3}$); asymmetry (As); skewness (Sk); kurtosis (Ku); snapshot of the free surface showing the multisoliton fission of long waves; bathymetric profile used in the simulation.

amplitudes ranging from 27 cm down to 0.01 cm. The complete distribution of soliton amplitudes is shown in Fig. 9. The resulting soliton energy ratio in the numerical experiment is 0.47.

Although there are some obvious differences between measured and modeled time series due to the mismatch between the numerical experiment and the measured wave field, we observe that the overall distribution of the detected solitons is quite similar. Most strikingly, both soliton energy ratios are very close to 0.5.

V. SUMMARY AND CONCLUSIONS

To summarize, in this article we have demonstrated that an SG can be formed in a natural coastal environment from ocean swells and identified a specific set of necessary conditions: first, the generation of surf-zone IGWs from incident narrow frequency band swells; second, a low-pass filtering effect at a bar-built estuary allowing only IGWs to enter into a shallow lagoon with Ursell numbers of order $U \sim 100$, leading to multisoliton fission of the primary long waves; and third, propagation of the resulting trains of solitons within a semienclosed shallow lagoon with gradually varying bathymetry that enhance intense wave-wave interactions. These conditions were only possible under a weak river discharge and subcritical flow conditions at the river mouth during flood tides; their coexistence might be just ephemeral and sporadic, making very difficult observing an SG dynamics in nature.

We recall that routes to SG and integrable turbulence have been theoretically studied over nearly 60 years since the seminal works of Zakharov [76] and Zabusky and Kruskal [2], but until now, such nonlinear wave regimes, leading to several orders of magnitude increase in the probability of encountering rogue waves, had only been reached in theoretical, numerical, and laboratory experiments.

ACKNOWLEDGMENTS

We acknowledge the support and collaboration of the Chilean “Ministerio del Medio Ambiente” (MMA), the United Nations Development Programme (UNDP) “GEF-Humedales Costeros de la Zona Centro-Sur de Chile, and the Municipality of Pichilemu; in particular, our gratitude goes to Claudia Silva, Luis Araya, and Cadudzzi Salas who were program coordinators at the national level and local levels at Laguna Cáhuil. We also thank Cabañas Piedra Grande at Villa Esperanza near Laguna Cáhuil and, in particular, Sebastián Arenas for their support for the deployment of the video cameras. The Corporación Punta de Lobos has to be acknowledged as well for facilitating some spaces and infrastructures during the development of the project. We also acknowledge Prof. Pablo Pastén from the Departamento de Ingeniería Hidráulica y Ambiental at the Escuela de Ingeniería UC for his kind support in the deployment of the 3 MHz Sontek RiverSurveyor S5 used in the field campaign. We also thank Prof. John D. Carter, from Seattle University, for providing the

KdV numerical model. The support of Efraín Magaña, Ph.D. student at Ingeniería UC, for stabilizing the drone videos, is also acknowledged. Discussions with Prof. John D. Carter, Prof. Eric Barthélemy, and Prof. Hervé Michallet on solitons and infragravity waves are greatly appreciated. This research has benefited from the financial support of the following grants of the Chilean National Research and Development Agency (ANID): ANID/FONDEF/ID22I10087, ANID /FONDAP/1523A0009, ANID/FONDECYT/1251583, ANID /FONDECYT/1231494, ANID/FONDECYT/11220663, and CORFO-MERIC 14CEI2-28228.

R.C. conceived the study. R.C., P.A.C., R.F., and M.G. designed the field campaign and conducted the experiments with the support of F.L., P.D., and R.G., F.L., and C.E. prepared and carried out the wave climate modeling. J.G., F.L., and P.D. prepared and postprocessed the remote sensing data. S.W. performed a nonlinear Fourier analysis to measured and modeled free surface time series. R.C. and J.G. conducted the numerical experiments using the SGN and KdV models. R.C., P.A.C., R.F., M.G., J.G., and S.W. analyzed the data and discussed the results. R.C. and P.A.C. co-wrote the main section. R.C., P.A.C., R.F., M.G., J.G., S.W., F.L., P.D., and R.G. prepared and co-wrote the Supplemental Material and the Methods section.

The authors declare no competing interests.

DATA AVAILABILITY

The dataset of the analyzed wave field (pressure time series and videos) is publicly available at Ref. [36].

[1] J. E. Allen, The early history of solitons (solitary waves), Phys. Scr. **57**, 436 (1998).

[2] N. J. Zabusky and M. D. Kruskal, Interaction of "solitons" in a collisionless plasma and the recurrence of initial states, Phys. Rev. Lett. **15**, 240 (1965).

[3] A. Hasegawa and Y. Kodama, *Solitons in Optical Communications* (Oxford University Press, Oxford, UK, 1995).

[4] F. Lederer, G. I. Stegeman, D. N. Christodoulides, G. Assanto, M. Segev, and Y. Silberberg, Discrete solitons in optics, Phys. Rep. **463**, 1 (2008).

[5] S. K. Turitsyn, J. E. Prilepsky, S. T. Le, S. Wahls, L. L. Frumin, M. Kamalian, and S. A. Derevyanko, Nonlinear Fourier transform for optical data processing and transmission: advances and perspectives, Optica **4**, 307 (2017).

[6] P. Marin-Palomo, J. N. Kemal, M. Karpov, A. Kordts, J. Pfeifle, M. H. P. Pfeiffer, P. Trocha, S. Wolf, V. Brasch, M. H. Anderson, R. Rosenberger, K. Vijayan, W. Freude, T. J. Kippenberg, and C. Koos, Microresonator-based solitons for massively parallel coherent optical communications, Nature (London) **546**, 274 (2017).

[7] V. D. Djordjevic and L. G. Redekopp, The fission and disintegration of internal solitary waves moving over two-dimensional topography, J. Phys. Oceanogr. **8**, 1016 (1978).

[8] A. R. Osborne, Nonlinear ocean waves and the inverse scattering transform, *Scattering*, edited by R. Pike and P. Sabatier (Academic Press, London, 2010), Vol. 97.

[9] A. Chabchoub, N. Hoffmann, and N. P. Akhmediev, Rogue wave observation in a water wave tank, Phys. Rev. Lett. **106**, 204502 (2011).

[10] M. J. Ablowitz and D. E. Baldwin, Nonlinear shallow ocean-wave soliton interactions on flat beaches, Phys. Rev. E **86**, 036305 (2012).

[11] M. Onorato, S. Residori, U. Bortolozzo, A. Montina, and F. T. Arecchi, Rogue waves and their generating mechanisms in different physical contexts, Phys. Rep. **528**, 47 (2013).

[12] A. Costa, A. R. Osborne, D. T. Resio, S. Alessio, E. Chrivì, E. Saggese, K. Bellomo, and C. E. Long, Soliton turbulence in shallow water ocean surface waves, Phys. Rev. Lett. **113**, 108501 (2014).

[13] A. Slunyaev, Persistence of hydrodynamic envelope solitons: Detection and rogue wave occurrence, Phys. Fluids **33**, 036606 (2021).

[14] I. Teutsch, M. Brühl, R. Weisse, and S. Wahls, Contribution of solitons to enhanced rogue wave occurrence in shallow depths: a case study in the southern North Sea, Nat. Hazards Earth Syst. Sci. **23**, 2053 (2023).

[15] N. J. Zabusky and C. J. Galvin, Shallow-water waves, the Korteweg-deVries equation and solitons, J. Fluid Mech. **47**, 811 (1971).

[16] H. Yeh, W. Li, and Y. Kodama, Mach reflection and KP solitons in shallow water, Eur. Phys. J.: Spec. Top. **185**, 97 (2010).

[17] I. Redor, E. Barthélemy, H. Michallet, M. Onorato, and N. Mordant, Experimental evidence of a hydrodynamic soliton gas, Phys. Rev. Lett. **122**, 214502 (2019).

[18] V. E. Zakharov, Kinetic equation for solitons, Sov. Phys. JETP **33**, 538 (1971).

[19] G. A. El and A. M. Kamchatnov, Kinetic equation for a dense soliton gas, Phys. Rev. Lett. **95**, 204101 (2005).

[20] P. Suret, S. Randoux, A. Gelash, D. Agafontsev, B. Doyon, and G. El, Soliton gas: Theory, numerics, and experiments, Phys. Rev. E **109**, 061001 (2024).

[21] A. E. Gennady, Soliton gas in integrable dispersive hydrodynamics, J. Stat. Mech.: Theory Exp. (2021) 114001.

[22] F. Mitschke, G. Steinmeyer, and A. Schwache, Generation of one-dimensional optical turbulence, Physica D **96**, 251 (1996).

[23] P. Walczak, S. Randoux, and P. Suret, Optical rogue waves in integrable turbulence, Phys. Rev. Lett. **114**, 143903 (2015).

[24] P. Suret, R. E. Koussaifi, A. Tikan, C. Evain, S. Randoux, C. Szwaj, and S. Bielawski, Single-shot observation of optical rogue waves in integrable turbulence using time microscopy, Nat. Commun. **7**, 13136 (2016).

[25] P. Suret, A. Tikan, F. Bonnefoy, F. Copie, G. Ducrozet, A. Gelash, G. Prabhudesai, G. Michel, A. Cazaubiel, E. Falcon, G. El, and S. Randoux, Nonlinear spectral synthesis of soliton gas in deep-water surface gravity waves, Phys. Rev. Lett. **125**, 264101 (2020).

[26] T. Leduque, E. Barthélemy, H. Michallet, J. Sommeria, and N. Mordant, Space–time statistics of 2D soliton gas in shallow

water studied by stereoscopic surface mapping, Exp. Fluids **65**, 84 (2024).

[27] G. Marcucci, D. Pierangeli, A. J. Agranat, R.-K. Lee, E. DelRe, and C. Conti, Topological control of extreme waves, Nat. Commun. **10**, 5090 (2019).

[28] S. Randoux, P. Walczak, M. Onorato, and P. Suret, Intermittency in integrable turbulence, Phys. Rev. Lett. **113**, 113902 (2014).

[29] S. Randoux, P. Walczak, M. Onorato, and P. Suret, Nonlinear random optical waves: Integrable turbulence, rogue waves and intermittency, Physica D **333**, 323 (2016).

[30] D. S. Agafontsev, S. Randoux, and P. Suret, Extreme rogue wave generation from narrowband partially coherent waves, Phys. Rev. E **103**, 032209 (2021).

[31] T. Congy, G. El, G. Roberti, A. Tovbis, S. Randoux, and P. Suret, Statistics of extreme events in integrable turbulence, Phys. Rev. Lett. **132**, 207201 (2024).

[32] V. E. Zakharov, Turbulence in integrable systems, Stud. Appl. Math. **122**, 219 (2009).

[33] See Supplemental Material at http://link.aps.org/supplemental/10.1103/9zhq-j1sj for contextual oceanographic, hydrographic and estuarine conditions during the reported field campaign.

[34] D. Khojasteh, S. Rao, S. McSweeney, R. Ibaceta, R. J. Nicholls, J. French, W. Glamore, J. L. Largier, J. Adams, M. G. Hughes, M. Barry, H. E. Power, J. Du, T. A. Tucker, R. Cienfuegos, P. A. Catalan, and D. Hanslow, Intermittent estuaries deserve global attention as vulnerable and vital ecosystems, Commun. Earth Environ. **6**, 443 (2025).

[35] R. Cienfuegos, P. A. Catalán, F. Lucero, P. Díaz, R. Flores, M. Guerra, F. Venegas, A. Ossandón, and L. Araya, Continuous interannual monitoring of artificial and natural breachings of an intermittently open/closed estuary in central Chile, in *Proceedings of the Coastal Dynamics 2025 Conference, Aveiro, Portugal* (Springer Nature, London, 2025).

[36] R. Cienfuegos, P. A. Catalan, R. Flores, M. Guerra, J. Galaz, E. Magaña, and F. Lucero, Dataset for "Soliton gas dynamics and rogue wave enhancement in a natural coastal environment" [Data set], Zenodo (2025), doi:10.5281/zenodo.17192781.

[37] P. Bonneton, D. Lannes, K. Martins, and H. Michallet, A nonlinear weakly dispersive method for recovering the elevation of irrotational surface waves from pressure measurements, Coastal Eng. **138**, 1 (2018).

[38] A. Grinsted, J. C. Moore, and S. Jevrejeva, Application of the cross wavelet transform and wavelet coherence to geophysical time series, Nonlinear Processes Geophys. **11**, 561 (2004).

[39] https://grinsted.github.io/wavelet-coherence/.

[40] S. Winder, *Analog and Digital Filter Design*, 2nd ed. (Elsevier, 2002).

[41] T. H. C. Herbers, S. Elgar, and R. T. Guza, Infragravity-frequency (0.005–0.05 Hz) motions on the shelf. Part I: Forced waves, J. Phys. Oceanogr. **24**, 917 (1994).

[42] T. H. C. Herbers, S. Elgar, R. T. Guza, and W. C. O'Reilly, Infragravity-frequency (0.005–0.05 Hz) motions on the shelf. Part II: Free waves, J. Phys. Oceanogr. **25**, 1063 (1995).

[43] A. Sheremet, R. T. Guza, S. Elgar, and T. H. C. Herbers, Observations of nearshore infragravity waves: Seaward and shoreward propagating components, J. Geophys. Res.: Oceans **107**, 10-1 (2002).

[44] X. Bertin *et al.*, Infragravity waves: From driving mechanisms to impacts, Earth-Sci. Rev. **177**, 774 (2018).

[45] M. J. Tucker and E. G. Pitt, *Waves in Ocean Engineering* (Elsevier, 2001), Vol. 5.

[46] J. Gemmrich and L. Cicon, Generation mechanism and prediction of an observed extreme rogue wave, Sci. Rep. **12**, 1718 (2022).

[47] K. T. Holland, R. A. Holman, T. C. Lippmann, J. Stanley, and N. Plant, Practical use of video imagery in nearshore oceanographic field studies, IEEE J. Oceanic Eng. **22**, 81 (1997).

[48] G. Bradski, The OpenCV library, Dr. Dobb's J. Software Tools **3** (2000).

[49] https://www.planet.com.

[50] E. Magaña, F. S. Costabal, and W. Brevis, Image velocimetry using direct displacement field estimation with neural networks for fluids, arXiv:2501.18641.

[51] I. Redor, H. Michallet, N. Mordant, and E. Barthélemy, Experimental study of integrable turbulence in shallow water, Phys. Rev. Fluids **6**, 124801 (2021).

[52] S. Trillo, G. Deng, G. Biondini, M. Klein, G. F. Clauss, A. Chabchoub, and M. Onorato, Experimental observation and theoretical description of multisoliton fission in shallow water, Phys. Rev. Lett. **117**, 144102 (2016).

[53] R. Cienfuegos, E. Barthélemy, and P. Bonneton, Wave-breaking model for Boussinesq-type equations including roller effects in the mass conservation equation, J. Waterw. Port Coastal Ocean Eng. **136**, 10 (2010).

[54] R. Cienfuegos, Surfing waves from the ocean to the river with the Serre-Green-Naghdi equations, J. Hydraul. Eng. **149**, 04023032 (2023).

[55] E. Mignot and R. Cienfuegos, On the application of a Boussinesq model to river flows including shocks, Coastal Eng. **56**, 23 (2009).

[56] J. D. Carter, D. Henderson, and P. Panayotaros, The spatial Whitham equation, J. Fluid Mech. **996**, A42 (2024).

[57] M. Brühl, P. J. Prins, S. Ujvary, I. Barranco, S. Wahls, and P. L.-F. Liu, Comparative analysis of bore propagation over long distances using conventional linear and KdV-based nonlinear Fourier transform, Wave Motion **111**, 102905 (2022).

[58] Y.-C. Lee, M. Brühl, and S. Wahls, When do JONSWAP spectra lead to soliton gases in deep water conditions? in *International Conference on Offshore Mechanics and Arctic Engineering* (American Society of Mechanical Engineers, 2023), Vol. 86878, p. V005T06A101.

[59] C. S. Gardner, J. M. Greene, M. D. Kruskal, and R. M. Miura, Method for solving the Korteweg-deVries equation, Phys. Rev. Lett. **19**, 1095 (1967).

[60] S. Wahls, S. Chimmalgi, and P. J. Prins, FNFT: A software library for computing nonlinear Fourier transforms, J. Open Source Software **3**, 597 (2018).

[61] P. J. Prins and S. Wahls, Reliable computation of the eigenvalues of the discrete KdV spectrum, Appl. Math. Comput. **433**, 127361 (2022).

[62] P. de Koster, M. Brühl, and S. Wahls, Water-depth identification from free-surface data using the KdV-based nonlinear Fourier transform, in *International Conference on Offshore Mechanics and Arctic Engineering* (American Society of Mechanical Engineers, 2022), Vol. 85901, p. V05BT06A056.

[63] S. L. McSweeney, J. C. Stout, and D. M. Kennedy, Variability in infragravity wave processes during estuary artificial

entrance openings, Earth Surf. Processes Landforms **45**, 3414 (2020).

[64] P. Müller, C. Garrett, and A. Osborne, Rogue waves, Oceanography **18**, 66 (2005).

[65] K. Dysthe, H. E. Krogstad, and P. Müller, Oceanic rogue waves, Annu. Rev. Fluid Mech. **40**, 287 (2008).

[66] D. Dutykh and E. Pelinovsky, Numerical simulation of a solitonic gas in KdVand KdV–BBM equations, Phys. Lett. A **378**, 3102 (2014).

[67] E. Pelinovsky and A. Sergeeva, Numerical modeling of the KdV random wave field, Eur. J. Mech. B Fluids **25**, 425 (2006).

[68] G. Symonds, D. A. Huntley, and A. J. Bowen, Two-dimensional surf beat: Long wave generation by a time-varying breakpoint, J. Geophys. Res.: Oceans **87**, 492 (1982).

[69] T. Moura and T. Baldock, Remote sensing of the correlation between breakpoint oscillations and infragravity waves in the surf and swash zone, J. Geophys. Res.: Oceans **122**, 3106 (2017).

[70] M. E. Williams and M. T. Stacey, Tidally discontinuous ocean forcing in bar-built estuaries: The interaction of tides, infragravity motions, and frictional control, J. Geophys. Res.: Oceans **121**, 571 (2016).

[71] X.-M. Li, A new insight from space into swell propagation and crossing in the global oceans, Geophys. Res. Lett. **43**, 5202 (2016).

[72] J. D. Carter and R. Cienfuegos, The kinematics and stability of solitary and cnoidal wave solutions of the Serre equations, Eur. J. Mech. B Fluids **30**, 259 (2011).

[73] D. Mitsotakis, D. Dutykh, and J. Carter, On the nonlinear dynamics of the traveling-wave solutions of the Serre system, Wave Motion **70**, 166 (2017).

[74] S. Tkachenko, S. Gavrilyuk, and K.-M. Shyue, Hyperbolicity of the modulation equations for the Serre–Green–Naghdi model, Water Waves **2**, 299 (2020).

[75] Y. Goda, *Random Seas and Design of Maritime Structures* (World Scientific Publishing Company, Singapore, 2010), Vol. 33.

[76] V. E. Zakharov, Weak turbulence in media with a decay spectrum, J. Appl. Mech. Tech. Phys. **6**, 22 (1965).